AGU PUBLICATIONS

JGR

Journal of Geophysical Research: Space Physics

RESEARCH ARTICLE

10.1002/2014JA020345

This article is a companion to *Hysell et al.* [2014] doi:10.1002/2014JA019889.

Key Points:

- ESF activity generally predictable from ground-based measurements at JRO
- Depletions in ESF simulations share features with radar imagery
- Depletions not reproduced in simulation may be of nonlocal origin

Correspondence to:
D. L. Hysell,
dlh37@cornell.edu

Citation:
Hysell, D. L., M. A. Milla, L. Condori, and J. W. Meriwether (2014), Data-driven numerical simulations of equatorial spread *F* in the Peruvian sector: 2. Autumnal equinox, *J. Geophys. Res. Space Physics*, *119*, 6981–6993, doi:10.1002/2014JA020345.

Received 28 JUN 2014
Accepted 6 AUG 2014
Accepted article online 11 AUG 2014
Published online 29 AUG 2014

Data-driven numerical simulations of equatorial spread *F* in the Peruvian sector: 2. Autumnal equinox

D. L. Hysell[1], M. A. Milla[2], L. Condori[2], and J. W. Meriwether[3]

[1]Earth and Atmospheric Sciences, Cornell University, Ithaca, New York, USA, [2]Jicamarca Radio Observatory, Lima, Peru, [3]Physics and Astronomy, Clemson University, Clemson, South Carolina, USA

Abstract An ongoing effort to simulate plasma instability in the equatorial ionosphere leading to equatorial spread *F* (ESF) in the American sector is described. Ionospheric state parameters including plasma number density and vector drift velocity profiles were measured at the Jicamarca Radio Observatory in the period between 20 September and 3 October 2013. Coherent radar backscatter from plasma irregularities was recorded simultaneously, and images of the irregularities were calculated using aperture synthesis methods. Neutral winds were measured by the red line Fabry-Perot interferometers at Jicamarca and Arequipa, Peru. A fully 3-D numerical simulation of ionospheric irregularities, initialized and forced using parameterizations derived from measurements and empirical models, was used to reproduce the ESF activity observed. Simulations were able to recover many of the features of the irregularities, although some important anomalies can be noted. ESF events in which the first appearance of radar plumes occurred either very early or very late were not reproduced in simulation and may be indicative of nonlocal influence.

1. Introduction

The term "equatorial spread *F*" (ESF) refers to broadband plasma turbulence produced by interchange instabilities in the equatorial *F* region ionosphere mainly in the postsunset sector. The resulting ionospheric irregularities affect radio wave reflection and refraction and cause diffraction and scattering, degrading the performance of radio communication, navigation, and imaging systems. This space weather phenomenon has received considerable attention in the literature for more than 75 years, with computational studies dominating the research for most of the last 40 years. Contemporary research in ESF was reviewed recently by *Woodman* [2009] and *Kelley et al.* [2011]. While the most important aspects of ESF are believed to be understood and the underlying dynamics are not thought to be chaotic, the ability to forecast the phenomenon remains elusive.

This paper reports on an ongoing numerical study of ESF outlined by *Hysell et al.* [2014]. The study involves making comprehensive measurements of the postsunset equatorial ionosphere on a campaign basis using instruments at and near the Jicamarca Radio Observatory. Measurements are made both of background state parameters and of ionospheric irregularities, should they occur. The background ionospheric data are then used to initialize and drive a 3-D numerical simulation of plasma instabilities in the equatorial ionosphere. Finally, the simulation results are evaluated against the irregularity observations. While falling short of forecasts, the studies are intended to examine whether the most important mechanisms at work in ESF are being considered and modeled properly. (Actual forecasts would require electric field and thermospheric wind predictions and a better understanding of the quiet time variability therein and are beyond the scope of our regional simulation effort.)

At Jicamarca, ionospheric plasma turbulence is monitored by analyzing coherent radar backscatter from meter-scale, field-aligned plasma density irregularities (FAIs). Presentations of coherent radar backscatter data in conventional range-time-intensity (RTI) format indicate the local times and altitudes where irregularities exist—see *Woodman and La Hoz* [1976]. At this stage in the study, we supplement RTI analysis with aperture synthesis imaging analysis (see *Hysell and Chau* [2006, and references therein] for review). Aperture synthesis provides true spatial images of backscatter from FAIs in the plane perpendicular to the geomagnetic field. The images can be compared more directly with numerical simulations to assess how well the simulations reproduce irregularity morphology and development.

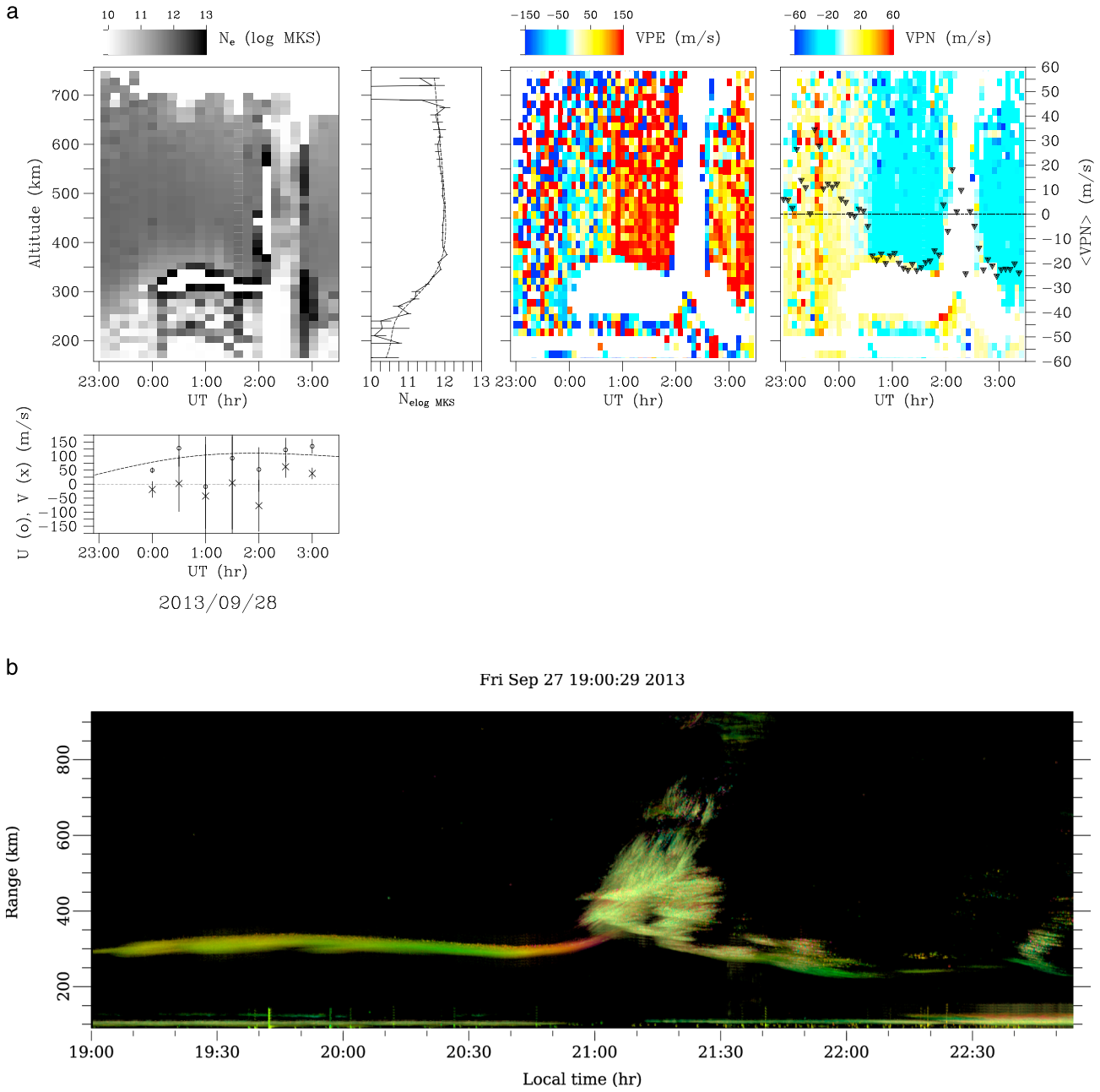

Figure 1. Jicamarca observations of ESF on 27/28 September 2013. (a) (first panel) Electron density, (second panel) electron density profiles at 2345 UT, (third panel) zonal plasma drifts, and (fourth panel) vertical plasma drifts. (fifth panel) Neutral winds at 250 km altitude. (b) Coherent backscatter. Note that UT = LT + 5 h.

New campaign data were acquired at Jicamarca between 20 September and 3 October 2013, and numerical simulations of the campaign data were conducted. Below, we review the data and the corresponding simulations. We also discuss how radar imagery can be used to help evaluate the simulations. We find that the simulations can recover the level of irregularity activity present on a given night and that the simulations are morphologically similar to the radar imagery. There are, however, inconsistencies and anomalies. In particular, large radar plumes with no obvious causes in the campaign data were observed.

2. Campaign Data

Data for this study were acquired at the Jicamarca Radio Observatory outside Lima, Peru, as well as at the optical station at Arequipa, Peru. The campaign took place between 20 September and 3 October

2013. The system noise temperature of the 50 MHz radar is dominated by the cosmic noise temperature which undergoes an order-of-magnitude diurnal variation with changing sidereal time. Since the galactic center is directly overhead in the postsunset sector during Autumnal equinox, the incoherent scatter signal-to-noise ratio is significantly degraded in that season. Furthermore, conditions for optical observing are also degraded with the approach of Southern Hemisphere summer. For the aforementioned reasons and also because of some technical considerations, we focus on just 3 days, 25–27 September, when all instruments were functioning and the optical and radar data quality was adequate for our study. These were geomagnetically quiet days for which the $F_{10.7}$ solar flux index was approximately 110.

Figure 1 is an example of the data used for this study. The data were acquired at Jicamarca using the observing mode described in detail by *Hysell et al.* [2014]. The first panel in Figure 1a shows electron density versus altitude and universal time (UT = LT + 5 h). In the second panel in Figure 1a is the electron density profile at 2345 UT (1845 LT) (solid line). Also plotted is the Parameterized Ionospheric Model (PIM) prediction for Jicamarca's location at 2345 UT (1845 LT) (dashed line)—see below. The third panel in Figure 1a depicts zonal plasma drifts, with positive numbers denoting eastward drifts. The fourth panel in Figure 1a shows vertical plasma drifts. The marker symbols represent height-averaged vertical drifts. The prereversal enhancement of the drifts maximized around 2330 UT (1830 LT), with the evening reversal occurring around 0030 UT (1930 LT). Small-scale plasma irregularities in the form of a bottom-type layer emerged at 0 UT (1900 LT), as indicated by the white spaces in the various panels where the echoes have been excised. A radar plume passed overhead from 0200 to 0230 UT (2100–2130 LT).

The fifth panel in Figure 1a shows time-averaged Fabry-Perot interferometer (FPI) wind measurements from Jicamarca. Here circle and cross symbols represent zonal and meridional drifts near the presumptive 250 km red line emission height, respectively. Measurements around the time of the evening reversal of the vertical plasma drifts generally exhibit large errors (when they are available at all) when the *F* layer is at its zenith and optical emissions become weak. Also plotted is the zonal neutral wind predicted by the horizontal wind model 07 (HWM07) at 250 km altitude for the prescribed scaling factor (dashed line)—see below.

Finally, Figure 1b presents coherent backscatter from plasma irregularities over Jicamarca in RTI format. The panel clearly shows a bottom-type layer at about 300 km altitude that persisted for 2 h before giving way to an ESF plume. Bottom-type layers are practically ubiquitous features of the postsunset *F* region over Jicamarca during equinox and December solstice. We regard the interval of the bottom-type layer as being a low-activity interval insofar as ESF is concerned. The occurrence of the plume is an anomaly that will be discussed later.

Figures 2 and 3 represent intervals with moderate and high levels of ESF activity, respectively. The neutral wind data shown for 26 September came from the Jicamarca FPI, whereas the data for 25 September came from the FPI at Arequipa where the observing conditions were better. Note that increased ESF activity implies increased coherent scatter and radar clutter and decreased amounts of time when useful incoherent scatter data are available. Note also that the high-activity event shown in Figure 3 is distinguished by the appearance of a radar plume at about 1910 LT (0010 UT), early in the evening, and prior to the formation of a bottom-type layer. Like the late evening plume in Figure 1, this too is statistically unusual and anomalous.

3. Numerical Simulations

Following the procedure of *Hysell et al.* [2014], we conducted numerical simulations of the events of 25–27 September in an attempt to recover the most salient features in the campaign data and to test our understanding of the mechanisms thought to be at work. The numerical code used is described in detail in that reference. In summary, it is a fully three-dimensional code that solves for the abundances of NO^+, O_2^+, O^+, and H^+ ions (and electrons) in the equatorial zone on the basis of forcing arising from electrostatic fields, winds, pressure, and gravity as an initial boundary value problem. The most computationally expensive part of the simulation is the calculation of the three-dimensional electrostatic potential, which satisfies the quasi-neutrality condition in the plasma. The simulation is cast in tilted magnetic dipole coordinates, with the dipole adjusted to match the magnetic declination in the Peruvian sector.

The simulation is started at 2345 UT with an initial specification of the ion abundances everywhere in space in a sector 10° in longitude wide, centered on Jicamarca's longitude. We use the PIM model [*Daniell et al.*, 1995] to specify the initial number density and the International Reference Ionosphere 2007 (IRI2007)

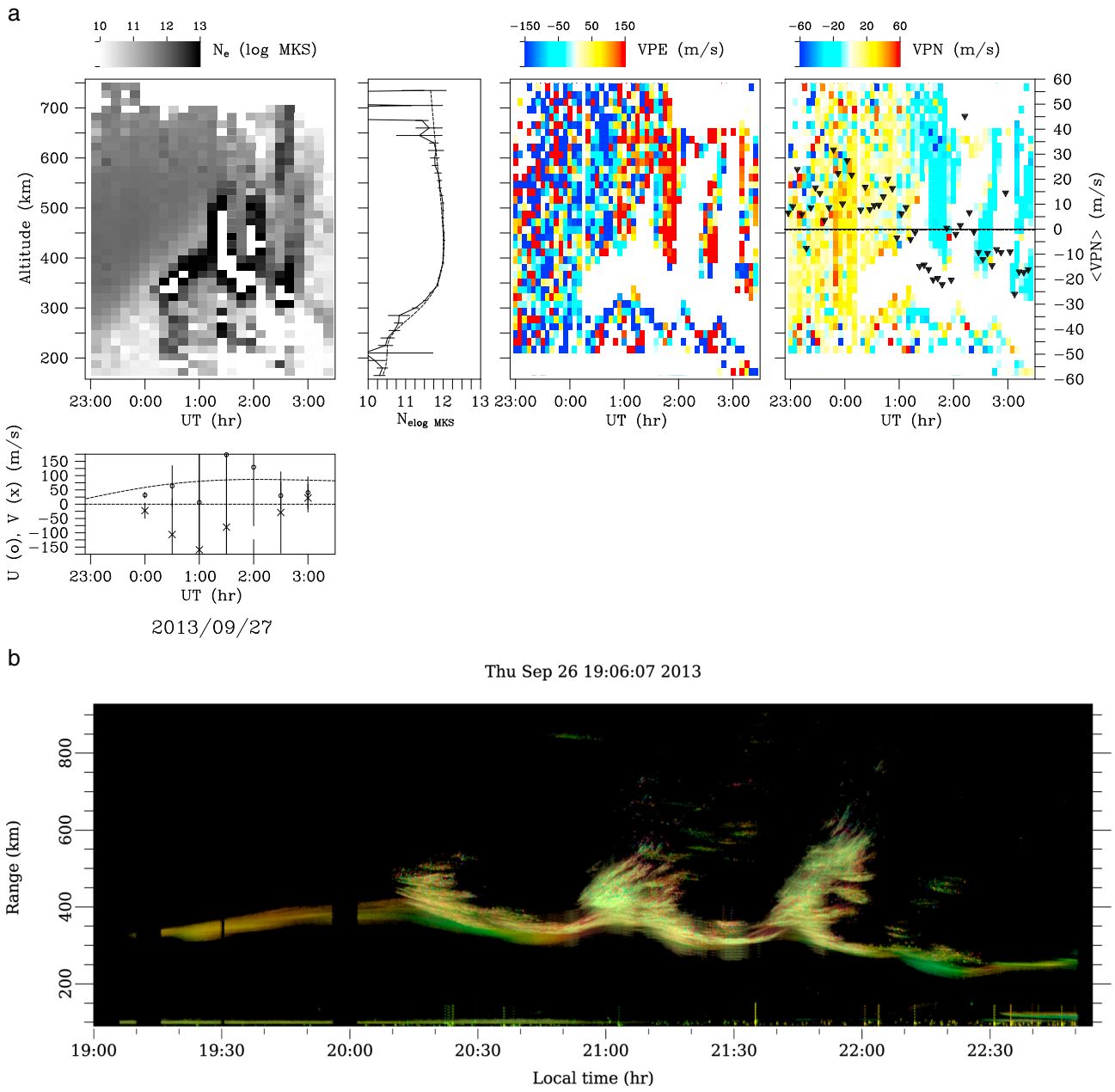

Figure 2. Same as Figure 1 except for 26/27 September 2013.

model [*Bilitza and Reinisch*, 2008] to specify the initial composition. (PIM number densities are more similar to density profiles measured by Jicamarca than IRI profiles, but PIM does not provide information about ion composition.) In order to capture day-to-day variability, we pass to PIM a proxy value for the $F_{10.7}$ solar flux index chosen to minimizes the model/data discrepancy at Jicamarca's location at 2345 UT. Our assumption here is that the initial specification at nearby latitudes, longitudes, and local times will also be reasonably accurate.

The PIM and IRI2007 models are not used again after initialization. As time progresses, forcing is applied through the specification of the background neutral winds and background zonal electric field. For the neutral winds, the HWM07 model is used [*Drob*, 2008]. In order to take into account day-to-day variability, we introduce a rescaling in the altitude parameter passed to HWM07:

$$h \leftarrow 100.0 + (h - 100.0) \times s$$

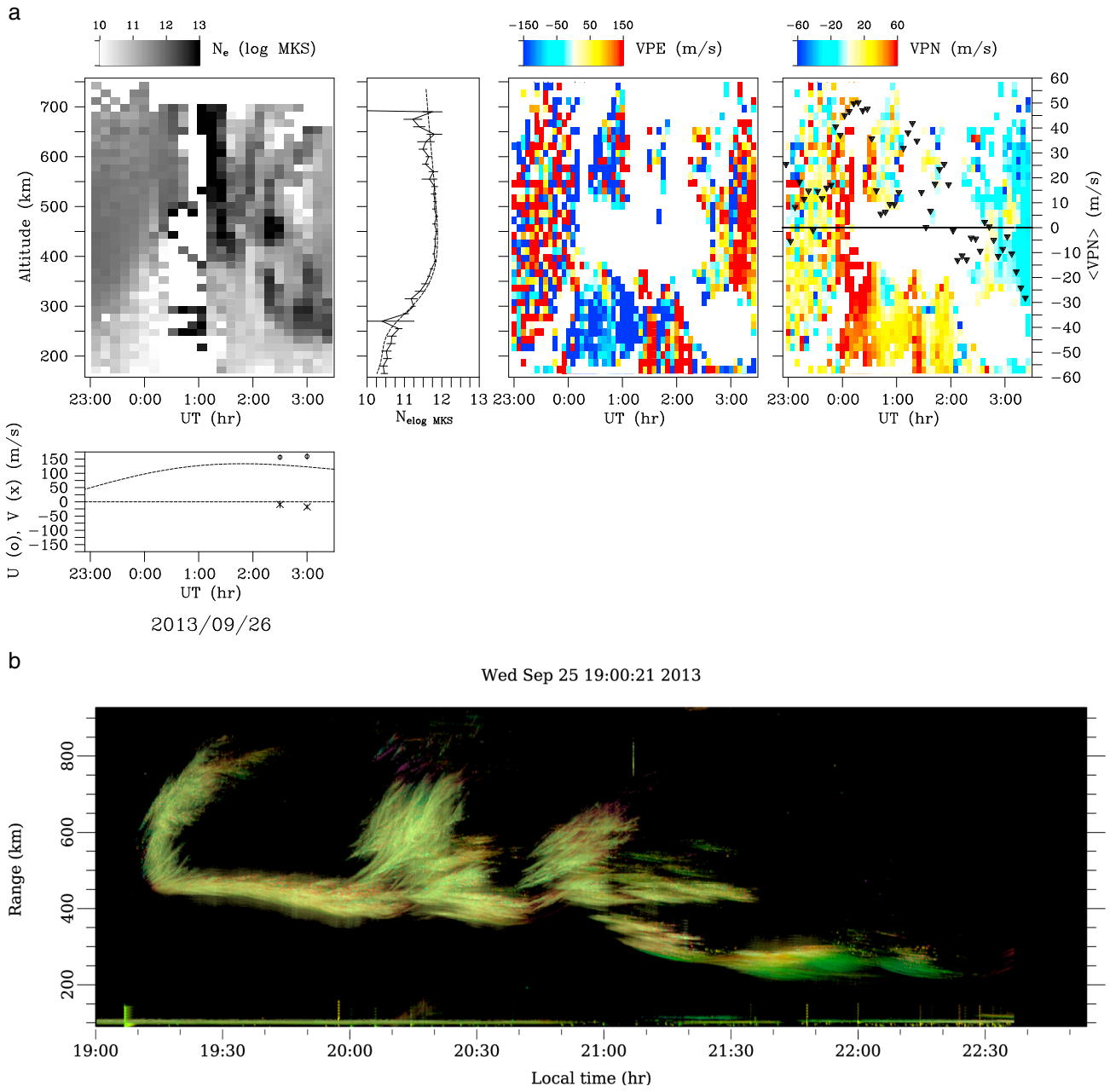

Figure 3. Same as Figure 1 except for 25/26 September 2013.

which stretches/compresses the altitude profile, moving the shear node closer to or further from the nominal 250 km altitude red line emission height. The scale factor s is set to bring about reasonable agreement with available red line FPI zonal wind data.

Finally, a specification of the background zonal electric field is provided by the ISR vertical drifts measurements. We fit the height-averaged vertical drifts observed between 2300 and 0200 UT (1800–2100 LT) to the formula

$$v_d(t) = v_o + v_1 \sin\left(2\pi \frac{t - t_o}{\tau}\right)$$

where t is universal time in hours. Here v_o, v_1, t_o, and τ set the offset, amplitude, phase, and period of the vertical drift, which varies nearly periodically around the time of the prereversal enhancement and evening

Table 1. Parameters Used to Specify Initialization and Forcing in the Numerical ESF Model for Different ESF Events Observed in the September 2013 Campaign

Event	PIM $F_{10.7}$	s	v_o	v_1	t_o	τ
25 Sept	145	1.75	24.5	14.0	23.7	2.17
26 Sept	135	1.00	−2.2	20.0	22.8	4.73
27 Sept	145	1.25	−3.3	19.7	22.7	3.35

reversal. We then set the background zonal electric field in the simulation according to v_d, converting from universal time to local time using the longitude of each simulation cell. Note that throughout initialization and forcing, local time and longitude are treated equivalently. Note also that our specification of the background zonal electric field is height invariant. *Pingree and Fejer* [1987] highlighted the requirement for altitude variation in the equatorial vertical drifts. We do not neglect this requirement but instead leave it to our potential solver to develop net vertical drifts that meet it.

Table 1 lists all of the parametrizations used for the simulation runs.

We perform data-driven simulations of the postsunset equatorial ionosphere in the Peruvian sector using the aforementioned procedures. White noise is added to the initial density specification in order to seed instability. Results for 27 September (low activity), 26 September (moderate activity), and 25 September 2013 (high activity) are shown in Figures 4–6, respectively. In each case, we simulate the ionosphere starting at 2345 UT (1845 LT), the approximate time of *F* region sunset. Simulations are carried out for 90 min. The nominal reversal time of the zonal background electric field makes it unlikely for ESF to begin at later times than we simulate, at least in simulation.

Figure 4 shows the results for the low-activity event. After 25 min, zonal currents driven by gravity and the zonal electric field dominate above about 400 km altitude. Below this, vertical currents associated with the imperfectly efficient *F* region dynamo dominate. These currents drive fast-growing interchange instabilities preferentially at the base of the *F* layer where there is significant vertical shear in the zonal plasma drifts [*Hysell and Kudeki*, 2004; *Kudeki et al.*, 2007]. The waves excited by this instability propagate obliquely with respect to the horizontal but cannot propagate far from the vertical current region. They are able to excite interchange instabilities driven by zonal currents and more commonly associated with ESF, but only so long as strong zonal currents are present. We associate the irregularities driven by vertical currents with bottom-type layers.

After 75 min, the background zonal electric field has reversed and is strongly westward. This inhibits instabilities capable of operating outside the vertical current region and necessary to produce depletion plumes and topside ESF. The bottom-type layer alone remains after 75 min and will continue to exist, by itself, so long as significant vertical current flows. The simulation appears to have reproduced the events of 27 September 2013 prior to the appearance of a radar plume (at 0200 UT) accurately.

The moderate-activity simulation shown in Figure 5 is similar to the low-activity run, the main difference being that the background zonal electric field remains eastward through the 75 min mark. By this time, the simulation predicts the development of modest depletion plumes propagating into the topside to nearly 500 km altitude. At such altitudes, the zonal currents driven by gravity are sufficiently strong to maintain irregularity growth and ascent even after the background electric field reverses. Simulations at later times indeed exhibit continued depletion development and ascent. This simulation appears to have captured accurately the events of 26 September 2013 leading to the appearance of the first ESF plume.

Finally, Figure 6 shows the results of the simulation for the high-activity event of 25 September 2013. The zonal electric field is much stronger throughout this simulation than in the previous two. The result is the rapid production of irregularities in the bottomside region that quickly extend into the topside and through the *F* peak. In this simulation, depletions encountered the upper simulation boundary and left the simulation space less than 60 min into the run. (The depletions at the top of the simulation at 75 min arrived there later.) This is consistent with the coherent scatter RTI data from 25 September, which show a large radar plume emerging from the bottomside, extending to nearly 600 km altitude, and passing overhead starting at about 0100 UT (2000 LT).

Of course, the RTI data also depict the passage of a well-developed radar plume starting at 1910 LT (0010 UT) or at about the 25 min mark in the simulation. Producing such well-developed irregularities so early in an ESF event is outside the capabilities of the simulation framework—see below.

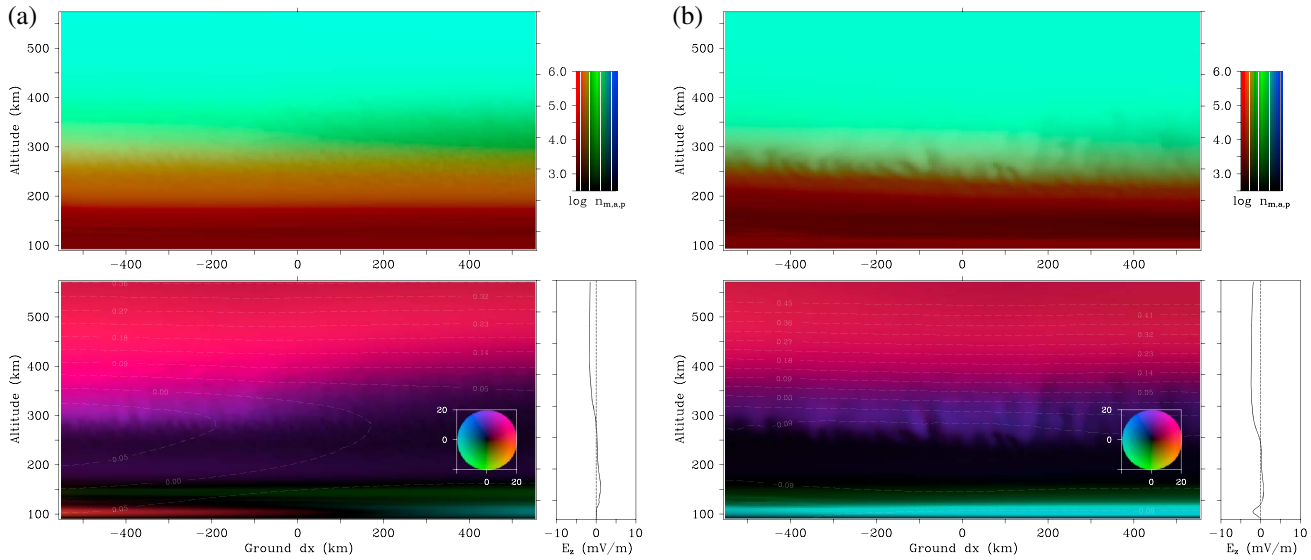

Figure 4. Numerical simulation of events on 27/28 September 2013 (low activity) initialized at 2345 UT. Simulated results after (a) 25 and (b) 75 min, respectively. Figures 4a and 4b (top) depict plasma number density, with red, green, and blue tones representing molecular, atomic, and protonic ion abundances, respectively. Figures 4a and 4b (bottom) show vector current density in the equatorial plane in nA/m^2 according to the legend shown. "Ground dx" or ground distance refers to the zonal displacement from the horizontal center of the simulation at ground level. White lines are equipotential contours, approximate streamlines of the flow. The vertical electric field through the center of the simulation is plotted in profiles to the right of the current density panels. Note that diamagnetic currents have no effect on dynamics and are not included in the current densities shown.

While the background zonal electric field more than any other parameter controls the overall rate of irregularity production in simulation, the zonal plasma drift profile is closely related to the morphology of the depletions that are produced. Different depletion spacings, tilts, widths, and secondary wave structuring can be produced systematically by changing the zonal neutral wind profile. It may ultimately be possible to extract diagnostic information about the thermospheric winds from these ESF plume characteristics. At Jicamarca, plume morphology can be studied using radar imaging.

4. Radar Imagery

To more completely evaluate the efficacy of the ESF simulations, we explore a new dimension of the problem by considering also the morphology of the simulated ESF events. For comparison, we examine images

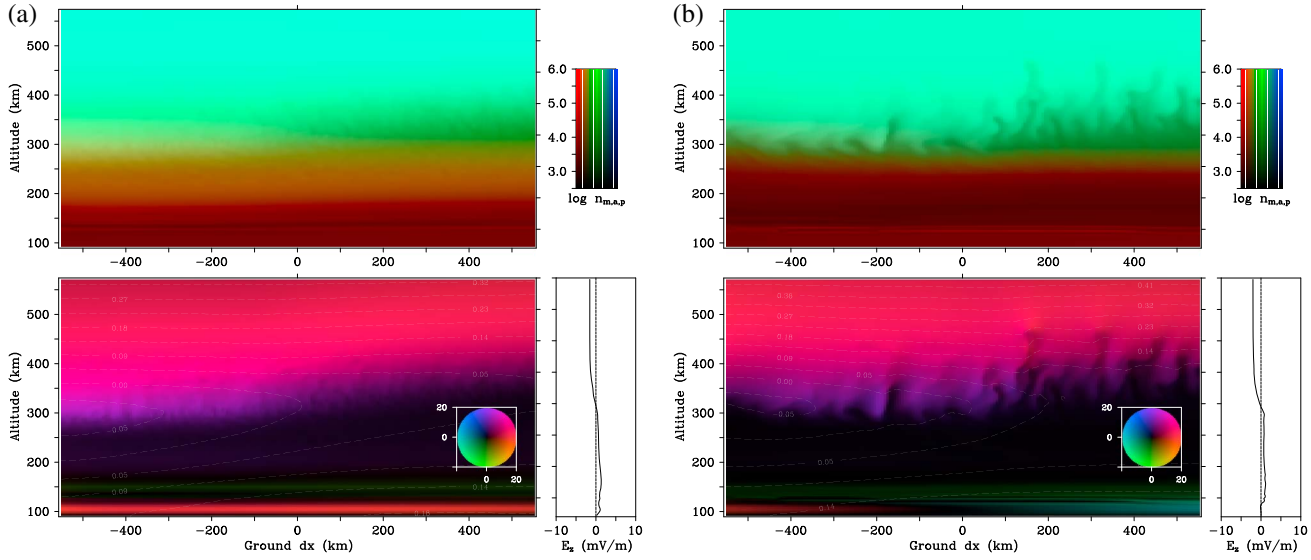

Figure 5. Same as Figure 4 except for 26/27 September 2013 (moderate activity).

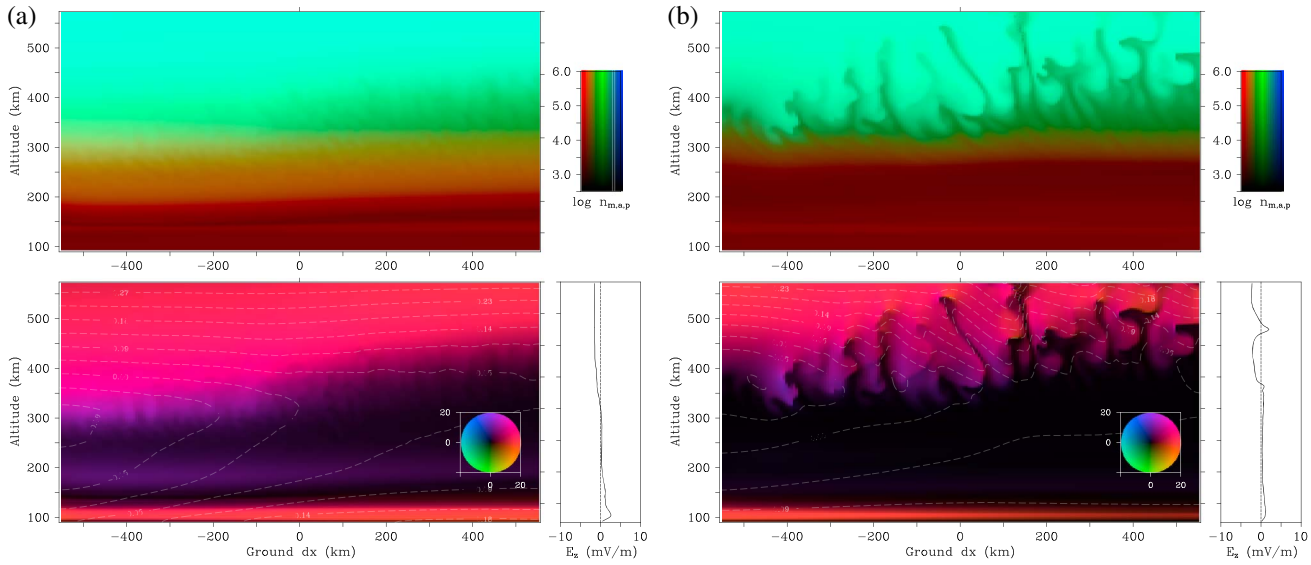

Figure 6. Same as Figure 4 except for 25/26 September 2013 (high activity).

of the coherent scatter radar plumes observed at Jicamarca constructed using aperture synthesis methods. Aperture synthesis techniques can be used to reveal the distribution of the radar backscatter versus bearing. By combining this information with range and Doppler information, the coherent scatter can be represented in a five-dimensional space (three spatial dimensions plus time and Doppler frequency). For field-aligned irregularities, the spatial dimension parallel to the magnetic field is not interesting for this study, and we consider only the two-dimensional perpendicular-to-B slice through the three-dimensional spatial volume. We will not utilize spectral information for this analysis and consider only the total signal-to-noise ratio, represented here by the brightness of the image pixels. While temporal information can be revealed by animating sequences of images, we will limit the analysis to a few still image frames. For more details about the methodology, see *Hysell and Chau* [2006, and references therein]. For the present experiments, reception was performed using eight antenna submodules (64ths) yielding 28 nonredundant interferometry baselines. Transmission was performed using a single submodule with a wide ($\sim 6°$) beam width.

Figures 7–9 show images of all the radar plumes observed from 25–27 September 2013. Each image shows backscatter signal-to-noise ratio versus range and azimuth in the equatorial plane for an incoherent integration period of about 10 s. (The hue and saturation of the pixels contain Doppler spectral information,

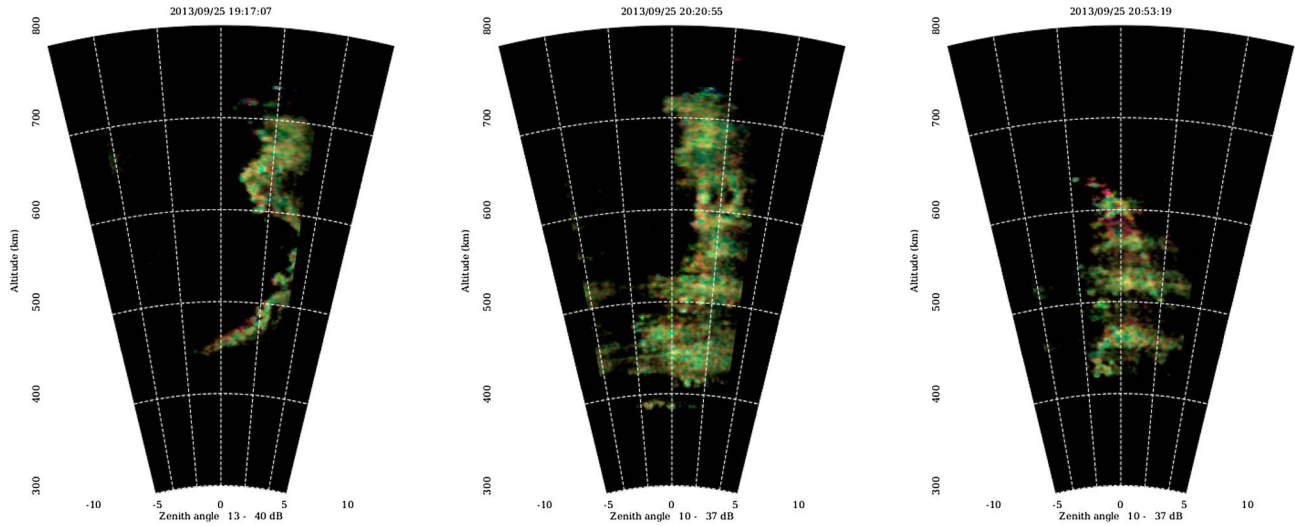

Figure 7. Aperture synthesis radar imagery for 25 September 2013 (high-activity case).

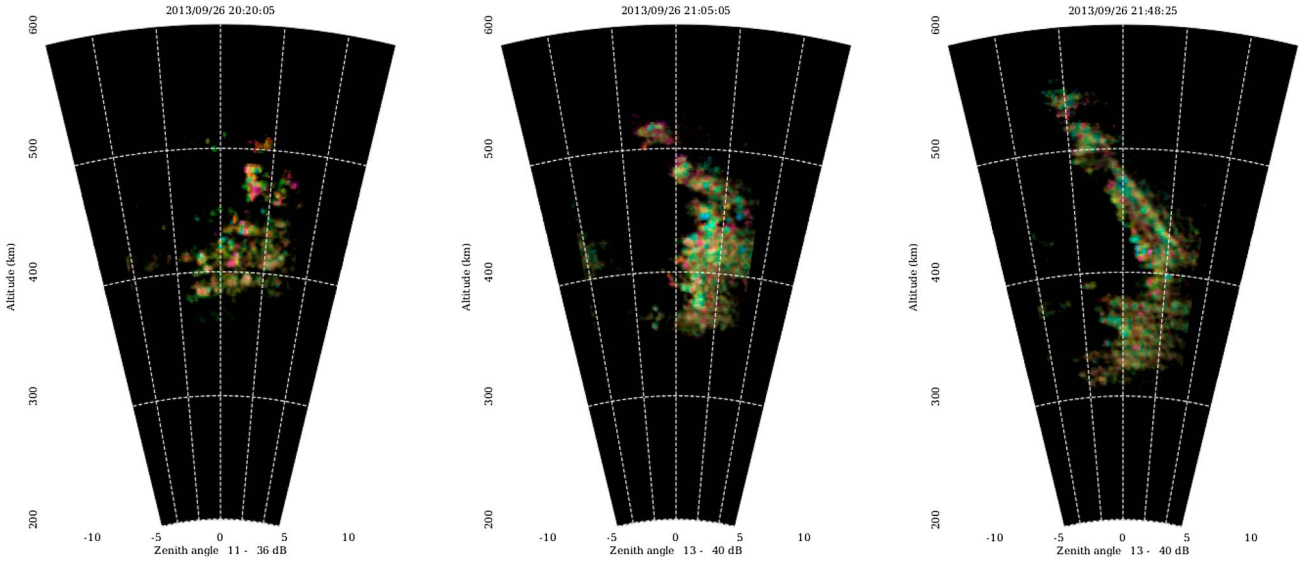

Figure 8. Aperture synthesis radar imagery for 26 September 2013 (moderate-activity case).

but we make no attempt to interpret that information here as mentioned above since most of the echoes are strongly frequency aliased.) The resolution of the pixels is finer than 1 km in either dimension. The images are snapshots in time of irregularities evolving under strongly inhomogeneous flows and undergoing rapid local creation and destruction. It would be incorrect to think of the depicted irregularities as drifting horizontally at uniform rates as if frozen into a uniform, steady background flow.

The intensity of the features in the images is indicative of the intensity of the part of the irregularity spectrum with vertical wave numbers and 3 m wavelengths. Comparison with in situ measurements suggests

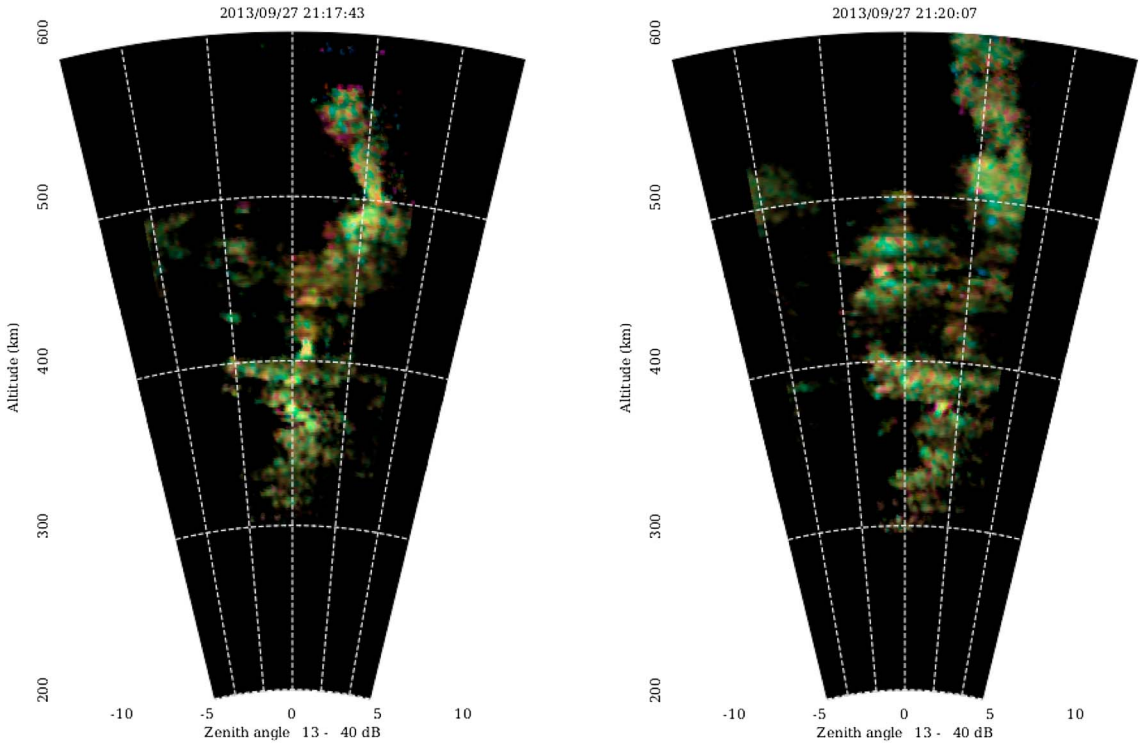

Figure 9. Aperture synthesis radar imagery for 27 September 2013 (low-activity case).

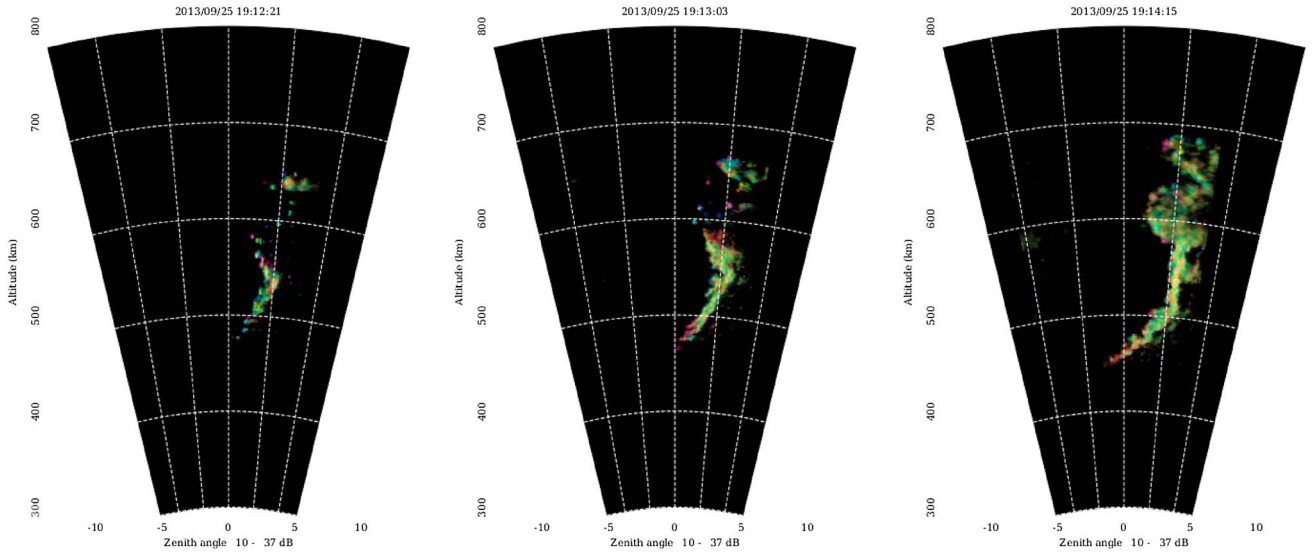

Figure 10. Aperture synthesis radar imagery for 25 September 2013 (first plume detail).

that the brightest features correspond to zones within the deepest density depletions where there are also steep vertical ledges [*Hysell et al.*, 2009]. While we assume that image features delineate the boundaries of large-scale plasma depletions, the absence of strong coherent backscatter does not necessarily imply the absence of depletions. There is therefore inherent uncertainty in what the coherent scatter images reveal about overall irregularity morphology.

At 50 MHz, coherent backscatter from radar plumes is typically much stronger than from bottom-type and bottomside layers. With the intensity scales applied here, backscatter from bottom-type layers is barely if at all visible.

The following characteristics are common to most radar plumes: (1) The plumes exhibit westward tilts and backward "C" shapes, with the tops and bottoms generally lying westward of the middle ranges. This feature is implied RTI maps [*Woodman and La Hoz*, 1976] and has been studied in detail and interpreted theoretically by *Zalesak et al.* [1982] and others. (2) The plumes are often characterized by narrow channels no more than a few kilometers wide. The flow speed within narrow channels can be arbitrarily large [*Aggson et al.*, 1992; *Huba and Joyce*, 2007]. (3) Secondary instabilities, highlighted by vertically stacked striations, are common. These are thought to indicate wind-driven instability on the walls of primary depletions [e.g., *Zalesak et al.*, 1982; *Tsunoda*, 1983]. (4) Secondary instabilities leading to bubble bifurcation also seem to be common [see *Zalesak et al.*, 1982; *Aggson et al.*, 1996; *Huba and Joyce*, 2007]. A bifurcated plume is evident in the two images in Figure 9. (In this case, the plume is wider than the imaging field of view, and so the two nearly sequential images have to be considered together.) Finally, it would be difficult to infer the information in Figures 7–10 from the RTI representations in Figures 1–3. RTI maps are suggestive but also misleading, and morphological comparisons between RTI maps and numerical simulations can engender spurious conclusions. For example, if one estimated the width of depletions from the product of their zonal drift rate and their duration in RTI maps, one would arrive at the width of the antenna beam used for coherent scatter, which is generally much broader than the width of the scattering regions.

Some considerations are important when comparing aperture-synthesis images with numerical simulations as well. The former are high-resolution images of regions of dense 3 m scatterers that suffer blurring effects due to radio scintillation. The latter or relatively coarse (an order of magnitude poorer spatial resolution) numerical estimates of plasma density that suffer from the limitations of the finite-volume simulation code.

Nevertheless, the simulated depletions are closer matches to the radar images than to the RTI presentations. The simulations moreover share image characteristics 1–4 enumerated above. The numerical simulations appear to be reproducing the most important features of ESF captured by the Jicamarca radar.

5. Evaluation

In most cases, the rate of development of the depletions in simulation is similar to what is observed in nature. Plumes in simulation reached nearly 500 km altitude by 2000 LT in the moderate-activity case and were observed at 500 km by 2010 LT over Jicamarca. Plumes ascended above 600 km by 1945 in the simulated high-activity case and were observed at 700 km by 2010 over Jicamarca. Only bottom-type layers emerged in the simulation of the low-activity case, and these were all that were observed at Jicamarca until 2100 LT.

The horizontal distance between plumes cannot be observed directly from the ground, but multiplying a nominal interplume interval of 45 min by a nominal zonal drift speed of 100 m/s yields a distance of 270 km. This figure is comparable to if somewhat larger than the interplume spacing observed for the highest depletions in the high-activity simulation case. The spacing between the dominant intermediate-scale depletions at the base of the *F* region in the low-activity simulation is meanwhile about 30–50 km. This figure matches the spacing between the patches of irregularities that constitute bottom-type layers in nature [*Hysell et al.*, 2005]. The simulation seems capable of producing the dominant ESF length scales produced in nature and predicted by asymptotic and transient linear analysis [*Hysell and Kudeki*, 2004; *Kudeki et al.*, 2007].

Furthermore, the most obvious features of radar plumes observed in aperture synthesis imagery can be found in the numerical simulations despite the limited basis for comparison. This overall model/data congruity suggests that much of the instability-related physics behind ESF is correctly incorporated in the numerical model. Improved congruity with the radar imagery in particular might be expected as a consequence of improving the spatial resolution of the simulation.

However, at least two results of the present study indicate that important physics is missing from the model considerations. The first is the radar plume that occurred late in the low-activity case featured in the RTI panel in Figure 1 and again in Figure 9. By the time the plume passed over Jicamarca, the background zonal electric field had been strongly westward for 90 min. The zonal electric field had never been strongly eastward, and so the likelihood of collisional interchange instability leading to topside ESF seems remote. The simulation predicted the existence of a bottom-type layer but could not have predicted the late plume. Late plumes like these are rare but not unknown occurrences at Jicamarca, particularly during low solar flux conditions (see *Hysell and Burcham* [1998] for statistics). We distinguish between layers which occur late and layers which occur after midnight. The latter are frequent in solar minimum but still poorly understood. They are beyond the scope of our current forecast efforts.

Our simulations are initialized using white noise as the seed and do not include any of the external factors often associated with day-to-day ESF variability such as gravity waves [e.g., *Kelley et al.*, 1981; *Huang and Kelley*, 1996; *Fritts et al.*, 2009; *Tsunoda*, 2010], ionization irregularities associated with the prereversal enhancement [*Sousasantos et al.*, 2013], sporadic *E* layers [*Batista et al.*, 2008] and associated *E* region plasma instabilities [*Tsunoda*, 2006], or so-called "large-scale wave structures" [*Tsunoda*, 2005]. Although not relevant here, storm-time phenomenology is also excluded. Still another consideration neglected by our studies is the effect of medium-scale traveling ionospheric disturbances (MSTIDs) propagating from middle latitudes and destabilizing the equatorial zone. This phenomenon has been observed directly by *Miller et al.* [2009] and modeled successfully by *Krall et al.* [2011] and so occupies center stage as a potential candidate for anomalous plume generation. Still another possibility is that the background conditions ~1000 km to the west of Jicamarca could have been very different than those considered in the simulation. Without regional knowledge of the background state and perturbations to it, discerning the cause of the late plume is impossible. Whatever the cause, it evidently left adjacent ionospheric regions unperturbed, as evidenced by the long-lived bottom-type layer over the observatory.

An even more challenging problem for the simulation is posed by the early radar plume seen on the active night and visible in the RTI panel of Figure 3 and again in Figures 7 and 10. In this case, a well-developed radar plume was observed by 1910 LT, shortly after *F* region sunset and without any precursor bottom-type layers. Such a phenomenon is exceptionally rare [*Hysell and Burcham*, 1998] and beyond the ability of our numerical simulation to recover absent extraordinarily strong initial forcing. There seems to be no rationale for applying strong forcing however; the vertical plasma drifts observed with incoherent scatter prior to the appearance of the plume were modest.

Another remarkable aspect of the early plume is that it appeared over Jicamarca in tact over the course of about 2 min rather than gradually drifting into the beam, which is the usual occurrence. Figure 10 shows three successive, closely spaced images of the plume. Backscatter became present suddenly after the plume had already passed over zenith. Within 2 min, the plume filled in between 450 and 700 km altitude, with backscatter at all altitudes appearing nearly simultaneously. Although convection is clearly present, animated imagery does not suggest plume formation by convection alone. The suggestion is rather of 3 m irregularities activating throughout a preexisting, large-scale depletion. This finding undermines the assumption that 3 m irregularities always accompany and delineate large-scale density depletions, complicating model validation.

As in the case of the late plume, a cause external to the immediate region and outside the present scope of the simulation is indicated for the early plume. Monitoring of the regions neighboring Jicamarca will evidently be necessary to account for similar anomalous events in ESF simulations.

6. Conclusions

We have extended the ESF simulation study begun by *Hysell et al.* [2014], applying the same methodology to data acquired in a campaign in Autumnal equinox, 2013, when ESF was more prevalent. Like before, we considered cases when ESF activity was relatively low, moderate, and high. By tuning the initialization and forcing of the simulation to match day-to-day background conditions, we were able to recover the various levels of activity observed experimentally. The overall match between simulations was reasonably close, qualitatively and in some ways quantitatively. The simulation correctly predicted the presence of bottom-type layers, modest ESF plumes, or large plumes over Jicamarca at about 2000 LT (1 UT) in each case. Plume height, separation, and overall morphology in simulation were comparable to what was seen in nature. In the future, the congruity between simulation and radar imagery might be improved by increasing the spatial resolution of the former, which is presently very coarse compared to the latter.

The simulations failed to reproduce two remarkable phenomena—a large radar plume that occurred late in the evening when the ionosphere appeared otherwise stable and another large plume that appeared very early in the evening without precursor layers or obvious drivers. It is difficult to conceive of a forecast strategy based solely on local ionospheric conditions that would have predicted either phenomena, which may have had sources outside the domain or scope of our simulations. As similar phenomena occur only rarely in the extensive coherent scatter database at Jicamarca, the overall strategy presented here is not seriously undermined. Going forward, however, instrumentation capable of sensing the regional background state and perturbations to it would seem to be required to improve congruity between observations and simulations.

Two experimental options in the Peruvian sector present themselves as a way forward. One is the network of dual-frequency GPS receivers and sounders fielded as part of the Low-Latitude Ionospheric Sensor Network (LISN) [*Valladares and Chau*, 2012]. Total electron content (TEC) traces and bistatic and multistatic ionospheric soundings in the Peruvian sector could be the basis for a real-time specification of large-scale irregularities such as MSTIDs propagating from middle latitudes that could inform the way the ESF simulations are initialized and driven. In addition to forecasting ESF manifestations in radar data, we can also begin use the LISN network to forecast GNSS outages, which are of greater practical importance. The LISN network is furthermore set to be augmented by a dense network of multistatic CW HF beacons in Peru. The beacons will use pseudorandom phase codes, interferometry, and GPS synchronization and yield information about the phase and group delay and bearing of the HF raypaths that connect them. This information too could be the basis for a regional ionospheric specification, able to inform the ESF simulations about irregularity sources that are not strictly overhead. We envision using the multistatic HF beacons to detect and track large-scale ionospheric perturbations propagating into the local field of view and initiating ESF events that cannot be anticipated through local modeling.

Acknowledgments
This work was supported by award FA9550-12-1-0462 from the Air Force Office of Scientific Research to Cornell University. The Jicamarca Radio Observatory is a facility of the Instituto Geofisíco del Perú operated with support from NSF award AGS-0905448 through Cornell. The help of the staff is much appreciated. Data used for this publication are available through the Madrigal database.

Michael Liemohn thanks Praveen Galav and an anonymous reviewer for their assistance in evaluating this paper.

References

Aggson, T. L., W. J. Burke, N. C. Maynard, W. B. Hanson, P. C. Anderson, J. A. Slavin, W. R. Hogey, and J. L. Saba (1992), Equatorial bubbles updrafting at supersonic speeds, *J. Geophys. Res.*, *97*, 8581–8590.

Aggson, T. L., H. Laasko, N. C. Maynard, and R. F. Pfaff (1996), In situ observations of bifurcation of equatorial ionospheric plasma depletions, *J. Geophys. Res.*, *101*(A3), 5125–5132, doi:10.1029/95JA03837.

Batista, I. S., M. A. Abdu, A. J. Carrasco, B. W. Reinisch, E. R. de Paula, N. J. Schuch, and F. Bertoni (2008), Equatorial spread F and sporadic E-layer connections during the Brazilian Conjugate Point Equatorial Experiment (COPEX), *J. Atmos. Sol. Terr. Phys.*, *70*, 1133–1143.

Bilitza, D., and B. W. Reinisch (2008), International reference ionosphere 2007: Improvements and new parameters, *Adv. Space Res.*, *42*, 599–609.

Daniell, R. E., L. D. Brown, D. N. Anderson, M. W. Fox, P. H. Doherty, D. T. Decker, J. J. Sojka, and R. W. Schunk (1995), PIM: A global parameterization based on first principles models, *Radio Sci.*, *30*, 1499–1510.

Drob, D. P. (2008), An empirical model of the Earth's horizontal wind fields: HWM07, *J. Geophys. Res.*, *113*, A12304, doi:10.1029/2008JA013668.

Fritts, D. C., et al. (2009), Overview and summary of the Spread *F* Experiment (SpreadFEx), *Ann. Geophys.*, *27*, 2141–2155.

Huang, C. S., and M. C. Kelley (1996), Nonlinear evolution of equatorial spread *F*: 1. On the role of plasma instabilities and spatial resonance associated with gravity wave seeding, *J. Geophys. Res.*, *101*, 283–292.

Huba, J. D., and G. Joyce (2007), Equatorial spread *F* modeling: Multiple bifurcated structures, large density "bite-outs," secondary instabilities, and supersonic flows, *Geophys. Res. Lett.*, *34*, L07105, doi:10.1029/2006GL028519.

Hysell, D. L., and J. Burcham (1998), JULIA radar studies of equatorial spread *F*, *J. Geophys. Res.*, *103*, 29,155–29,167.

Hysell, D. L., and J. L. Chau (2006), Optimal aperture synthesis radar imaging, *Radio Sci.*, *41*, RS2003, doi:10.1029/2005RS003383.

Hysell, D. L., and E. Kudeki (2004), Collisional shear instability in the equatorial *F* region ionosphere, *J. Geophys. Res.*, *109*, A11301, doi:10.1029/2004JA010636.

Hysell, D. L., M. F. Larsen, C. M. Swenson, A. Barjatya, T. F. Wheeler, M. F. Sarango, R. F. Woodman, and J. L. Chau (2005), Onset conditions for equatorial spread *F* determined during EQUIS II, *Geophys. Res. Lett.*, *32*, L24104, doi:10.1029/2005GL024743.

Hysell, D. L., R. B. Hedden, J. L. Chau, F. R. Galindo, P. A. Roddy, and R. F. Pfaff (2009), Comparing *F* region ionospheric irregularity observations from C/NOFS and Jicamarca, *Geophys. Res. Lett.*, *36*, L00C01, doi:10.1029/2009GL038983.

Hysell, D. L., R. Jafari, M. A. Milla, and J. W. Meriwether (2014), Data-driven numerical simulations of equatorial spread *F* in the Peruvian sector, *J. Geophys. Res. Space Physics*, *119*, 3815–3827, doi:10.1002/2014JA019889.

Kelley, M. C., M. F. Larsen, C. LaHoz, and J. P. McClure (1981), Gravity wave initiation of equatorial spread *F*: A case study, *J. Geophys. Res.*, *86*, 9087–9100.

Kelley, M. C., J. J. Makela, O. de la Beaujardiere, and J. Retterer (2011), Convective ionospheric storms: A review, *Rev. Geophys.*, *49*, RG2003, doi:10.1029/2010RG000340.

Krall, J., J. D. Huba, S. L. Ossakow, G. Joyce, J. J. Makela, E. S. Miller, and M. C. Kelley (2011), Modeling of equatorial plasma bubbles triggered by non equatorial traveling ionospheric disturbances, *Geophys. Res. Lett.*, *38*, L08103, doi:10.1029/2011GL046890.

Kudeki, E., A. Akgiray, M. A. Milla, J. L. Chau, and D. L. Hysell (2007), Equatorial spread-*F* initiation: Post-sunset vortex, thermospheric winds, gravity waves, *J. Atmos. Sol. Terr. Phys.*, *69*(17-18), 2416–2427.

Miller, E. S., J. J. Makela, and M. C. Kelley (2009), Seeding of equatorial plasma depletions by polarization electric fields from middle latitudes: Experimental evidence, *Geophys. Res. Lett.*, *36*, L18105, doi:10.1029/2009GL039695.

Pingree, J. E., and B. G. Fejer (1987), On the height variation of the equatorial *F* region vertical plasma drifts, *J. Geophys. Res.*, *92*, 4763–4766.

Sousasantos, J., E. A. Kherani, and J. H. Sobral (2013), A numerical simulation study of the collisional-interchange instability seeded by the pre-reversal vertical drift, *J. Geophys. Res. Space Physics*, *118*, 7438–7449, doi:10.1002/2013JA018803.

Tsunoda, R. T (1983), On the generation and growth of equatorial backscatter plumes: 2. Structuring of the west walls of upwellings, *J. Geophys. Res.*, *88*, 4869–4874.

Tsunoda, R. T. (2005), On the enigma of day-to-day variability in equatorial spread *F*, *Geophys. Res. Lett.*, *32*, L08103, doi:10.1029/2005GL022512.

Tsunoda, R. T. (2006), Day-to-day variability in equatorial spread *F*: Is there some physics missing?, *Geophys. Res. Lett.*, *33*, L16106, doi:10.1029/2006GL025956.

Tsunoda, R. T. (2010), On seeding equatorial spread *F*: Circular gravity waves, *Geophys. Res. Lett.*, *37*, L10104, doi:10.1029/2010GL043422.

Valladares, C. E., and J. L. Chau (2012), The Low-Latitude Ionosphere Sensor Network: Initial results, *Radio Sci.*, *47*, RS0L17, doi:10.1029/2011RS004978.

Woodman, R. F. (2009), Spread *F*: An old equatorial aeronomy problem finally resolved?, *Ann. Geophys.*, *27*, 1915–1934.

Woodman, R. F., and C. La Hoz (1976), Radar observations of *F* region equatorial irregularities, *J. Geophys. Res.*, *81*, 5447–5466.

Zalesak, S. T., S. L. Ossakow, and P. K. Chaturvedi (1982), Nonlinear equatorial spread *F*: The effect of neutral winds and background Pedersen conductivity, *J. Geophys. Res.*, *87*, 151–166.